

Metal-rich Damped/sub-Damped Lyman- α Quasar Absorbers at $z < 1$ [★]

C. Péroux^{1†}, J. D. Meiring², V. P. Kulkarni², R. Ferlet³, P. Khare⁴, J. T. Lauroesch⁵, G. Vladilo⁶, & D. G. York⁷.

¹ European Southern Observatory, Garching-bei-München, Germany.

² Dept. of Physics and Astronomy, Univ. of South Carolina, Columbia, USA.

³ Institut d’Astrophysique de Paris, UMR7095 CNRS, Université Pierre & Marie Curie, France.

⁴ Dept. of Physics, Utkal University, Bhubaneswar, India.

⁵ Dept. of Physics and Astronomy, Northwestern University, Evanston, USA.

⁶ Osservatorio di Trieste, Trieste, Italy.

⁷ Dept. of Astronomy and Astrophysics, Univ. of Chicago, Chicago, USA.

Accepted 2006 July 25. Received 2006 July 24; in original form 2006 April 04

ABSTRACT

Damped Lyman- α absorbers (DLAs), seen in absorption against a background quasar, provide the most detailed probes available of element abundances in the Universe over $> 90\%$ of its age. DLAs can be used to observationally measure the global mean metallicity in the Universe and its evolution with time. Paradoxically, these observations are more difficult at lower redshifts, where the absorber rest-frame UV spectra are cut-off due to the atmospheric absorption. We present here high-resolution VLT/UVES observations of several elements contained in three DLAs and one sub-DLA with $0.6 < z_{\text{abs}} < 0.9$. We detect Mg I, Mg II, Fe II, Zn II, Cr II, Mn II, Ti II and Ca II. Our observations more than double the high-resolution sample of [Zn/H] at $z < 1$. We also report the discovery of three metal-rich systems, whereas most previous measurements show low N_{HI} -weighted mean metallicity projecting to about 1/6th solar level at $z=0$. We derive $[\text{Zn}/\text{H}] = -0.11 \pm 0.04$ at $z_{\text{abs}} = 0.725$, $[\text{Zn}/\text{H}] = -0.54 \pm 0.20$ at $z_{\text{abs}} = 0.740$ and $[\text{Zn}/\text{H}] = -0.49 \pm 0.22$ at $z_{\text{abs}} = 0.652$, plus one additional upper limit ($[\text{Zn}/\text{H}] < -0.36$ at $z_{\text{abs}} = 0.842$). These measurements confirm the existence of quasar absorbers with relatively high metallicities based on abundance estimates free from the effect of dust depletion. Possible implications of these results for the metallicity of neutral gas phase in the past ≈ 8 Gyr are presented and compared with models.

Key words: Galaxies: abundances – intergalactic medium – quasars: absorption lines – quasars: individual: SDSS J0134+0051, SDSS J0256+0110, SDSS J1107+0048, SDSS J2328+0022

1 INTRODUCTION

Damped Lyman- α systems (DLAs) seen in absorption in the spectra of background quasars are selected over all redshifts independent of the intrinsic luminosities of the underlying galaxies. They have hydrogen column densities, $\log N_{\text{HI}} \gtrsim 20.3$ and are major contributors to the neutral gas in the Universe (Péroux et al. 2003). The DLAs offer direct probes

of element abundances over $> 90\%$ of the age of the Universe. In particular, the element Zn is only mildly depleted onto dust grains and is known to trace Fe in most Galactic stars with $[\text{Fe}/\text{H}] \geq -3$ (e.g. Mishenina et al. 2002; Cayrel et al. 2004). Zinc is thus an excellent tracer of the total metallicity in quasar absorbers (e.g., Pettini, et al. 1997; Kulkarni, Fall, & Truran 1997; Péroux et al., 2002; Khare et al. 2004). Iron, on the other hand, is often depleted out of gas phase onto dust grains, and so, is not a good tracer of metallicity in the interstellar medium of other galaxies. By comparing the gas phase abundance of refractory elements such as Fe, Mn, Cr, etc. to that of Zn, one can assess the quantity of interstellar grains in the systems.

Most chemical evolution models (e.g., Malaney &

[★] Based on observations collected during programme ESO 74.A-0597 at the European Southern Observatory with UVES on the 8.2 m KUEYEN telescope operated at the Paranal Observatory, Chile.

[†] e-mail: cperoux@eso.org

Chaboyer, 1996; Pei, Fall, & Hauser, 1999) predict the global metallicity of the Universe to rise from nearly zero at high z to nearly solar at $z = 0$ although galaxy to galaxy variation may be expected from the mass-metallicity relation (Tremonti et al. 2004; Savaglio et al. 2005) as well as from gradients of abundance with galaxy radius (i.e. Ellison, Kewley & Mallén-Ornelas, 2005; Chen et al. 2005; Zwaan et al. 2005). The present-day mass-weighted mean metallicity of local galaxies is also nearly solar (e.g., Kulkarni, & Fall, 2002; Fukugita & Peebles 2004). The N_{HI} -weighted metallicity of DLAs is expected to follow this behaviour if they trace an unbiased sample of absorbers selected only by $N(\text{HI})$. However, studies of the cosmological evolution of the H I column density-weighted mean metallicity in DLAs shows surprising results. Contrary to most models of cosmic chemical evolution, recent observations suggest a relatively mild evolution in DLA global metallicity with redshift for $0 \lesssim z \lesssim 4$ (Prochaska et al. 2003; Khare, et al., 2004; Kulkarni, et al., 2005; Meiring et al. 2006 and references therein). Treating Zn limits with survival analysis, Kulkarni et al. (2005) obtained a slope of -0.18 ± 0.07 and an intercept (i.e., projected metallicity at $z = 0$) of -0.79 ± 0.18 for the metallicity-redshift relation. Similar values for the slope have been reported from previous Zn samples (-0.26 ± 0.10 ; Kulkarni & Fall 2002), and from a larger heterogeneous sample of Zn, Fe, Si, S, and X-ray absorption measurements (-0.25 ± 0.07 ; Prochaska et al. 2003). Overall the N_{HI} -weighted mean metallicity of DLAs is less than $1/10^{\text{th}}$ solar at $z=2$ and about $1/6^{\text{th}}$ solar at $z=1$ (Meiring et al. 2006).

These results suggest that the global mean DLA metallicity stays far below the solar level at all redshifts. However, the exact shape of the metallicity-redshift relation is still not accurately determined. This uncertainty is mainly due to the small number of measurements available at $z < 1.5$, which corresponds to $\sim 70\%$ of the age of the Universe. In fact, most of the low-redshift data available so far are based on low-resolution spectroscopy. Only 2 DLAs with $z < 1$ have been measured at high resolution, a DLA at $z=0.68$ (de La Varga & Reimers 2000) and a DLA at $z=0.86$ (Pettini et al. 2000). This is primarily because (a) for $z < 0.6$, Zn II lines lie in the UV and can only be accessed with HST (which currently has no high-resolution spectrograph working), and (b) for $0.6 < z < 1.5$, Zn II lines lie in the blue wavelengths where most spectrographs have relatively low sensitivities. Yet, high resolution is important both for lowering the detection threshold and for resolving blends of Mg I and Cr II and the two Zn II lines at $\lambda\lambda 2026, 2062$ which are separated by 50 km/s and 62 km/s respectively. Fortunately, new low-redshift DLAs are being discovered rapidly. The 100,000 quasar spectra being obtained in the Sloan Digital Sky Survey (SDSS) combined with HST observations (and future facilities) are expected to increase the number of DLAs by an order of magnitude (York et al. 2000; Rao & Turnshek 2000; York, et al. 2001; York et al. 2005). It is important to determine the elemental abundances in these DLAs which probe a large fraction of the age of the Universe.

Here, we present VLT/UVES high-resolution spectra for 4 absorbers at $z < 1$ which allow us to study their velocity structure, to discern potential saturation effects, and thus to determine the variation of metallicity and dust content among the various velocity components. The paper is organised as follows: section 2 refers to the target selection

and data reduction processes. The analysis of every individual system is detailed in section 3, while section 4 describes the abundance determination and potential impact on our understanding of the metallicity evolution of the Universe.

2 OBSERVATIONAL STRATEGY AND DATA REDUCTION

In order to assess the metallicity of the Universe at $z < 1$, we have started in autumn 2002 a campaign aimed at measuring abundances in low- z systems. We have considered the low- z DLAs and sub-DLA systems (i.e. systems with $\log N_{\text{HI}} > 19.0$ as first defined by Péroux et al. 2003) with known N_{HI} discovered with either the Hubble Space Telescope ($0.1 < z < 0.6$) or Sloan ($0.6 < z < 1.5$) and followed up with the Multiple Mirror Telescope (MMT), e.g., Khare et al. 2004; Kulkarni et al. 2005; Meiring et al. 2006. These systems were chosen in the first place because their N_{HI} is known from HST data and they have strong Fe II and Mg II lines in the Sloan spectra. Given that these systems were chosen because of strong metal lines, they are probably predisposed to be more metal rich. We have acquired high-resolution observations of the most promising systems in order to determine the exact velocity profiles and to remove blends of lines of different elements (e.g. contribution of Mg I $\lambda 2026.5$ from that of Zn II $\lambda 2026.1$, and of Zn II $\lambda 2062.7$ from Cr II $\lambda 2062.2$). From this sample, a super-solar sub-DLA was discovered (Khare et al. 2004). Our high-resolution follow-up study of this sight line has shown that it is the most metal-rich DLA/sub-DLA known to date (Péroux et al. 2006).

The new sample presented here consists of 3 DLAs and 1 sub-DLA at $0.6 < z < 0.9$. The data were acquired with the Ultraviolet and Visual Echelle Spectrograph (UVES) mounted on Kueyen Unit 2 Very Large Telescope (D'Odorico et al. 2000). The observations were performed in Service Mode in period 74 between October 2004 and March 2005 under program number ESO 74.A-0597. We used a combination of 346+564 and 390+564 nm central wavelength settings appropriate to the range of wavelengths of the lines we are seeking. The total exposure time for each object was split into two or three equal observing blocks to minimize the effect of cosmic rays. A 2×2 CCD binning was used all along. The properties of the targets and the dates of observations are summarised in Table 1. The names of the targets are abbreviated throughout the paper. The full names are respectively: SDSS J013405.75+005109.4, SDSS J025607.24+011038.6, SDSS J110729.03+004811.1 and SDSS J232820.37+002238.2.

The data were reduced using the most recent version of the UVES pipeline in MIDAS (uves/2.1.0 flmidas/1.1.0). Master bias and flat images were constructed using calibration frames taken closest in time to the science frames. The science frames were extracted with the “optimal” option. The spectrum was then corrected to vacuum heliocentric reference. The resulting spectra were combined weighting each spectrum with its signal-to-noise ratio. The resulting spectral resolution is $R = \lambda / \Delta \lambda \sim 45000$. To perform the abundance studies, the spectra were divided into 50–75 Å regions, and each region was normalised using cubic spline functions of orders 1 to 5 as the local continuum.

Table 1. Dates of observations of our programme to study the total metallicity (free from the effect of dust bias) of $z_{\text{abs}} < 1$ quasar absorbers.

Quasar	g mag	z_{em}	z_{abs}	$\log N_{\text{HI}}^a$	Obs Date	UVES settings (nm)	Exp. Time (sec)
SDSS J0134+0051	18.33	1.522	0.842	$19.93^{+0.10}_{-0.15}$	19/21 Oct 2004	346+564	3×4800
SDSS J0256+0110	18.96	1.348	0.725	$20.70^{+0.11}_{-0.22}$	21/22 Oct 2004 + 11 Nov 2004	390+564	3×5400
SDSS J1107+0048	17.66	1.388	0.740	$21.00^{+0.02}_{-0.05}$	11 Jan 2005 + 1 Mar 2005	390+564	2×3600
SDSS J2328+0022	18.01	1.309	0.652	$20.32^{+0.06}_{-0.07}$	02 Oct 2004	390+564	3×5300

^a: N_{HI} measurements are from Rao, Turnshek, & Nestor (2006) for SDSS J0256+0110, SDSS J1107+0048, and SDSS J2328+0022, and from Rao (2005, private communication) for SDSS J0134+0051.

3 ANALYSIS

The column densities were estimated by fitting multi-component Voigt profiles to the observed absorption lines using the program FITS6P (Welty, Hobbs, & York 1991) which evolved from the code used by Vidal-Madjar et al. (1977). FITS6P minimizes the χ^2 between the data and the theoretical Voigt profiles convolved with the instrumental profile. On some occasions, **fitylman** in MIDAS (Fontana & Ballester 1995) was used to allow for simultaneous fits of several lines of the same ions (i.e. Fe II). The fits were performed assuming that metal species with similar ionisation potentials can be fitted using identical velocities and Doppler b parameters. The redshifts are measured from the Sloan spectra (York et al. 2005). The atomic data were adopted from Morton (2003).

For the fitting procedure, the same prescription was used for all the systems. The velocity and Doppler b parameters of the various components were estimated from the Mg I, Mg II, and Fe II lines and then kept fixed for the remaining lines, allowing for variations from one metal species to another in N only. In all cases, the Mg I $\lambda 2026.5$ contribution to the Zn II $\lambda 2026.1$ line was estimated using the component parameters for Mg I derived from the Mg I $\lambda 2852$ profile. For the four quasar absorbers under study, the Mg II $\lambda\lambda 2796$ and 2803 profiles were fitted together, but provide only a lower limit to Mg II owing to saturation in the central components. In Tables 2 to 5, the resulting column densities in the few weak components that could not be well-constrained due to noise are marked with ‘-’; their contributions to the total column densities are negligible and therefore not included in the total sum. These are nevertheless listed for consistency with the velocity structure of the strong lines of Fe II and Mg II. We also report rest-frame equivalent widths (hereafter EW) for Mg I, Mg II, Zn II, Cr II and Ca II together with their 1σ photon noise uncertainties. York et al. (2006) suggest that Mg I $\lambda 2026$ is unimportant to the Zn II $\lambda 2026$ analysis if $\text{EW}(\text{Mg I } \lambda 2852) < 0.60 \text{ \AA}$. Above this threshold, Mg I $\lambda 2026$ competes with Zn II $\lambda 2026$ or could even overwhelm it. But below that, it appears that the individual components that make up strong Mg I lines are not saturated. Since the ratio of oscillator strengths for the two Mg I transitions is 32, an unsaturated Mg I component seen in $\lambda 2852$ would be difficult to detect at $\lambda 2026$. We verify this result in several particular cases at high resolution. We have also checked the

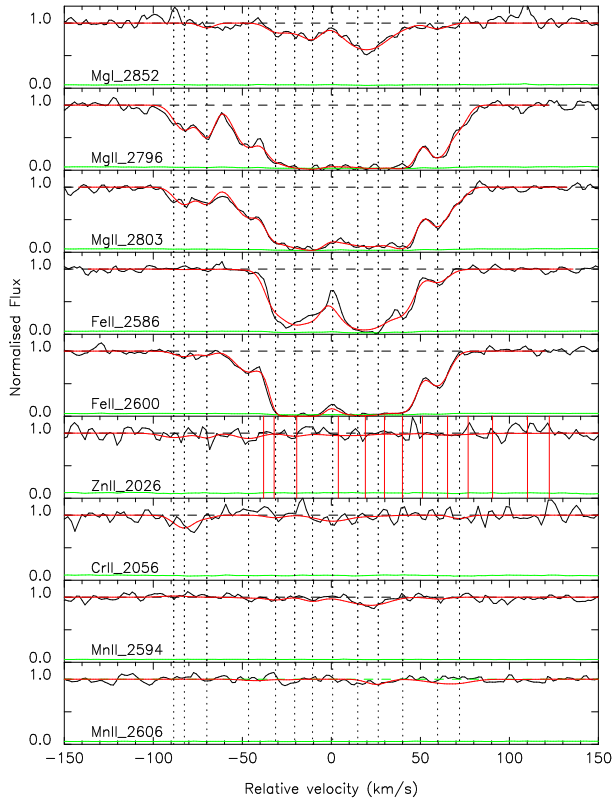


Figure 1. Velocity plots of the various lines covered at $z_{\text{abs}} = 0.842$ toward SDSS J0134+0051. The dotted vertical lines indicate positions of the components while the solid vertical lines in the Zn II $\lambda 2026$ panel indicate the position of the Mg I $\lambda 2026$ components. The solid grey line near the zero flux level is the error array.

Sloan spectra of our objects for the presence of systems that might contain lines that would blend with the lines which are being analysed here. A catalogue of the Sloan systems is being created (York et al., 2005) where many lines have been identified and double checked with our high-resolution spectra.

Table 2. Parameter fit to the $z_{\text{abs}} = 0.842$ SDSS J0134+0051 sub-DLA line. Velocities and b values are in km s^{-1} and column densities are in cm^{-2} . The σ values below the column densities are the error estimates on the column densities.

	Vel	b	Mg I	Mg II	Fe II	Zn II	Cr II	Mn II
N(X)	-88.5	9.9	—	—	—	4.38E+11	—	—
σ	—	—	—	3.72E+11	—	—
N(X)	-82.6	7.4	—	1.87E+12	8.17E+11	—	5.38E+12	—
σ	—	1.13E+11	2.63E+11	—	1.94E+12	—
N(X)	-69.9	5.3	5.56E+10	1.28E+12	4.28E+11	2.90E+11	—	—
σ	2.32E+10	9.70E+10	1.40E+11	1.84E+11	—	—
N(X)	-46.5	9.1	—	4.48E+12	3.21E+12	5.35E+11	—	—
σ	—	1.72E+11	2.37E+11	2.36E+11	—	—
N(X)	-31.3	6.9	1.26E+11	8.47E+12	1.25E+13	—	—	2.84E+11
σ	3.10E+10	4.68E+11	8.60E+11	—	—	1.24E+11
N(X)	-20.6	7.7	1.37E+11	>1.33E+13	7.10E+13	—	—	—
σ	3.68E+10	...	5.32E+12	—	—	—
N(X)	-10.5	6.8	2.35E+11	>1.44E+13	3.01E+13	—	—	4.27E+11
σ	4.13E+10	...	2.84E+12	—	—	1.51E+11
N(X)	0.7	11.5	—	>1.11E+13	—	2.14E+11	—	—
σ	—	...	—	3.83E+11	—	—
N(X)	14.8	12.2	6.14E+11	>1.44E+13	8.93E+13	—	—	9.03E+11
σ	8.02E+10	...	7.35E+12	—	—	2.66E+11
N(X)	26.3	10.9	3.98E+11	>1.36E+13	6.00E+13	—	—	9.12E+11
σ	6.65E+10	...	6.17E+12	—	—	2.27E+11
N(X)	40.1	8.1	6.00E+10	1.61E+13	2.53E+13	—	—	—
σ	3.37E+10	8.04E+11	1.40E+12	—	—	—
N(X)	59.7	7.6	9.14E+10	5.66E+12	6.57E+12	—	—	2.02E+11
σ	2.82E+10	2.01E+11	2.95E+11	—	—	1.19E+11
N(X)	72.0	5.9	—	8.89E+11	—	—	1.07E+12	—
σ	—	1.02E+11	—	—	9.79E+11	—

3.1 SDSS J0134+0051, $z_{\text{em}}=1.522$, $z_{\text{abs}}=0.842$

Voigt profile fitting to the Ly- α absorption line in the HST STIS spectra for this object (program 9382, PI: Rao) gives $\log N_{\text{HI}} = 19.93$ for this absorber (Sandhya Rao, *private communication*). In line with other N_{HI} measurements reported here, the error estimate for the column density of this system is derived by moving the continuum level above and below the best-fit continuum and re-doing the Voigt profile fitting using the `fitlyman` package within `MIDAS` (Fontana & Ballester 1995). This gives $\log N_{\text{HI}} = 19.93^{+0.10}_{-0.15}$.

At $z_{\text{abs}}=0.842$, Mg I λ 2852, Mg II $\lambda\lambda$ 2796 and 2803, Fe II $\lambda\lambda$ 2586 and 2600, Zn II $\lambda\lambda$ 2026 2056, Cr II $\lambda\lambda$ 2056 and 2062 and Mn II $\lambda\lambda$ 2594 and 2606 are covered. The absorption profiles show a complex velocity structure with a total of 13 components needed to properly fit the observed profile. Figure 1 presents the resulting fits and the parameters are given in Table 2. Listed are the N and σN values for each component of each ion.

The rest-frame EW of these lines are measured to be: EW(Mg I λ 2852)= $0.23\pm0.01\text{\AA}$, EW(Mg II λ 2796)= $1.15\pm0.01\text{\AA}$ and EW(Mg II λ 2803)= $0.96\pm0.01\text{\AA}$. So the Mg I contribution to the λ 2026 line, shown by the solid vertical lines of the Zn II λ 2026 panel in Figure 1, should be negligible. The Fe II column densities in the components at extreme negative velocities were constrained by using the Fe II $\lambda\lambda$ 2586 and 2600 lines simultaneously, since they are weak in the other Fe II lines. Zn II, Cr II and the two Mn II are extremely weak in some components and therefore lead to upper limits on the total column density estimates.

In addition, this rich quasar spectrum has a strong absorption system at $z_{\text{abs}}=0.618$. This system is most likely a DLA or sub-DLA given the strength of the Fe II $\lambda\lambda$ 2249, 2260, 2344, 2374, 2382 and Ti II λ 3384 lines in our spectra. Unfortunately, its Ly- α absorption line lies in a region of the HST spectrum where the quasar flux is very low owing to the Lyman limit absorption from another system at $z = 1.272$. Thus it is not possible to estimate the N_{HI} for the $z = 0.618$ system. Based on Ly- α line for the $z = 1.272$ system, we estimate that it has $\log N_{\text{HI}}$ in the range 18.9 to 19.1. This other system at $z_{\text{abs}}=1.272$ shows very strong C IV and Mg II doublets, Si II λ 1526, Al II λ 1670, Mg I λ 2852, Fe II $\lambda\lambda$ 1608, 2374, 2382, 2600. Also another absorber is detected at $z_{\text{abs}}=1.449$ with strong Si IV doublet, Si II λ 1526, C II λ 1334, Ni II λ 1370, C IV doublet and Fe II λ 2600.

3.2 SDSS J0256+0110, $z_{\text{em}}=1.348$, $z_{\text{abs}}=0.725$

Voigt profile fitting to the Ly- α absorption line in the HST STIS spectra for this object (Rao, Turnshek & Nestor, 2006) give $\log N_{\text{HI}} = 20.70^{+0.11}_{-0.22}$. Mg I λ 2852, Mg II $\lambda\lambda$ 2796 and 2803, Fe II $\lambda\lambda$ 2249, 2260, 2374, 2382, 2586 and 2600, Zn II λ 2026, Zn II+Cr II λ 2062, Mn II $\lambda\lambda$ 2576, 2594 and 2606 and Ti II λ 3384 are detected in this system. The absorption profiles show a complex velocity structure with a total of 19 components needed to best fit the profile. The results of the profile fitting analysis are summarised in Table 3, while Figure 2 and Figure 3 illustrate the fits. Strong C IV is also

Table 3. Parameter fit to the $z_{\text{abs}} = 0.725$ SDSS J0256+0110 DLA line. Velocities and b values are in km s^{-1} and column densities are in cm^{-2} . The σ values below the column densities are the error estimates on the column densities.

	Vel	b	Mg I	Mg II	Fe II	Zn II	Cr II	Mn II	Ti II
N(X)	-140.9	8.9	—	—	1.02E+10	—	5.38E+11	3.94E+11	—
σ	—	—	1.25E+09	—	1.57E+12	1.20E+11	—
N(X)	-118.7	8.5	4.66E+10	9.33E+11	5.49E+13	—	3.23E+12	—	—
σ	2.07E+10	1.68E+11	1.28E+12	—	1.65E+12	—	—
N(X)	-98.9	11.1	4.77E+10	2.14E+13	7.41E+10	—	—	—	1.51E+11
σ	2.53E+10	1.11E+12	1.73E+09	—	—	—	7.23E+10
N(X)	-81.1	9.2	8.48E+11	>4.28E+13	8.51E+11	5.72E+11	—	1.29E+12	—
σ	3.81E+10	...	1.98E+10	3.47E+11	—	1.43E+11	—
N(X)	-47.3	17.1	1.81E+12	>1.08E+14	1.02E+14	2.16E+12	4.53E+12	4.66E+12	—
σ	5.66E+10	...	2.38E+12	5.05E+11	2.30E+12	2.16E+11	—
N(X)	-23.8	9.4	4.70E+11	>9.41E+12	1.23E+14	—	3.71E+12	5.31E+11	—
σ	3.76E+10	...	5.79E+12	—	1.89E+12	1.42E+11	—
N(X)	-1.2	14.0	1.37E+12	>1.27E+14	2.82E+14	1.33E+12	8.81E+12	1.88E+12	1.32E+11
σ	4.79E+10	...	6.72E+12	4.44E+11	2.31E+12	1.67E+11	7.84E+10
N(X)	31.0	10.2	9.29E+11	>6.35E+13	5.13E+13	7.55E+11	7.90E+12	1.59E+12	4.81E+11
σ	3.99E+10	...	7.60E+12	3.76E+11	2.03E+12	1.47E+11	7.08E+10
N(X)	52.8	10.6	9.93E+11	>1.01E+14	1.70E+14	3.19E+12	9.98E+12	2.50E+12	3.67E+11
σ	4.06E+10	...	8.01E+12	4.94E+11	2.14E+12	1.61E+11	7.06E+10
N(X)	77.8	6.5	7.59E+11	>4.91E+13	3.16E+14	2.08E+12	2.50E+09	1.23E+12	—
σ	3.96E+10	...	2.26E+13	4.32E+11	1.44E+12	1.25E+11	—
N(X)	97.2	13.6	1.14E+12	8.20E+13	1.35E+14	3.49E+12	8.02E+12	1.58E+12	—
σ	4.34E+10	4.57E+12	3.14E+12	5.39E+11	2.31E+12	1.62E+11	—
N(X)	138.4	8.6	2.47E+11	1.12E+13	3.55E+08	5.18E+11	6.28E+12	—	2.16E+11
σ	2.39E+10	4.21E+11	1.67E+07	3.34E+11	2.15E+12	—	6.30E+10
N(X)	157.8	9.5	3.13E+10	2.23E+12	—	—	4.28E+12	3.15E+11	2.03E+11
σ	2.16E+10	1.73E+11	—	—	2.09E+12	1.23E+11	6.60E+10
N(X)	179.6	10.5	—	8.32E+11	6.92E+12	—	—	—	1.11E+11
σ	—	1.49E+11	1.61E+11	—	—	—	6.78E+10
N(X)	207.0	11.6	—	1.11E+13	6.16E+12	—	—	2.07E+11	—
σ	—	3.55E+11	1.40E+11	—	—	1.32E+11	—
N(X)	236.1	10.8	1.02E+11	4.61E+12	—	—	—	—	9.07E+10
σ	2.35E+10	2.14E+11	—	—	—	—	6.82E+10
N(X)	256.3	7.6	2.72E+10	2.22E+12	5.89E+13	3.68E+11	2.97E+12	1.36E+11	—
σ	1.93E+10	1.67E+11	1.37E+12	3.03E+11	1.54E+12	1.09E+11	—
N(X)	274.8	6.4	2.66E+11	2.68E+13	3.55E+13	3.39E+11	3.79E+12	5.88E+11	—
σ	2.25E+10	2.05E+12	1.67E+12	2.83E+11	1.50E+12	1.08E+11	—
N(X)	289.3	5.3	3.62E+11	1.39E+13	—	6.58E+11	—	6.57E+11	9.03E+10
σ	2.42E+10	9.57E+11	—	2.85E+11	—	1.03E+11	4.91E+10

detected at $z_{\text{abs}}=1.326$ with associated Fe II $\lambda 1608$ in the same UVES spectrum.

At $z_{\text{abs}}=0.725$, the rest-frame EW of these lines are measured to be: EW(Mg I $\lambda 2852$)= $0.94\pm 0.01\text{\AA}$, EW(Mg II $\lambda 2796$)= $3.22\pm 0.01\text{\AA}$, EW(Mg II $\lambda 2803$)= $2.88\pm 0.01\text{\AA}$, EW(Zn II $\lambda 2026$)= $0.24\pm 0.02\text{\AA}$ and EW(Zn II+Cr II $\lambda 2062$)= $0.23\pm 0.02\text{\AA}$ while Cr II $\lambda 2056$ is not detected. We have carefully checked that these detections/non-detections are self-consistent considering the respective oscillator strengths and noise in the appropriate region. In this system, the Mg I $\lambda 2852$ line provides a good guide to the component decomposition. Many Fe II lines are detected; the weakest ones are used to constrain the most central components of the profile while the strongest lines are used to accurately determine the column density in the weaker components. The component at -1.2 km s^{-1} seems broader in Mg I $\lambda 2852$ than in Fe II $\lambda 2374$. Similarly, the saturated Fe II lines show a very weak extra component at $v=-140.9 \text{ km s}^{-1}$ not seen in the other elements. Zn II+Mg I $\lambda 2026$

and Zn II+Cr II $\lambda 2062$ are clearly detected and lead to robust column density determinations. The solid vertical lines in the Zn II $\lambda 2026$ and Cr II $\lambda 2062$ panels of Figure 3 indicate the position of the Mg I $\lambda 2026$ and Zn II $\lambda 2062$ components respectively. Mn II and Ti II are also unambiguously detected and accurate column densities could be determined.

3.3 SDSS J1107+0048, $z_{\text{em}}=1.388$, $z_{\text{abs}}=0.740$

Voigt profile fitting to the Ly- α absorption line in the HST STIS spectra for this object (Rao, Turnshek & Nestor, 2006) give $\log N_{\text{HI}}=21.00_{-0.05}^{+0.02}$. This system was first studied by Khare et al. (2004) who reported abundance determination for various elements. In the new high-resolution data, several lines are detected in this system including Mg I $\lambda 2852$, Mg II $\lambda\lambda 2796$ and 2803 , Fe II $\lambda\lambda 2249, 2260, 2374, 2382$ and 2586 , Zn II $\lambda 2026$, Cr II $\lambda\lambda 2056$ and 2062 and Mn II $\lambda 2576$. The velocity profile is best fitted with 15 components. Figure 4

Table 4. Parameter fit to the $z_{\text{abs}} = 0.740$ SDSS J1107+0048 DLA line. Velocities and b values are in km s^{-1} and column densities are in cm^{-2} . The σ values below the column densities are the error estimates on the column densities.

	Vel	b	Mg I	Mg II	Fe II	Zn II	Cr II	Mn II
N(X)	-186.8	6.8	6.22E+10	9.15E+12	1.17E+13	—	—	—
σ	1.64E+10	3.97E+11	3.39E+12	—	—	—
N(X)	-166.6	6.6	1.21E+11	1.19E+13	—	—	8.0992E+12	3.60E+11
σ	1.74E+10	6.34E+11	—	—	3.1904E+12	2.11E+11
N(X)	-150.6	7.2	1.97E+11	1.25E+13	1.70E+13	—	—	—
σ	1.97E+10	6.08E+11	2.97E+12	—	—	—
N(X)	-112.5	6.4	4.99E+10	1.90E+13	8.91E+12	—	—	6.59E+11
σ	1.60E+10	1.36E+12	2.57E+12	—	—	2.20E+11
N(X)	-88.6	12.0	7.24E+11	>6.31E+13	5.62E+14	2.45E+12	1.1855E+13	2.33E+12
σ	3.03E+10	...	2.65E+13	7.55E+11	4.0125E+12	3.30E+11
N(X)	-66.0	10.8	4.05E+11	>5.03E+13	2.04E+14	1.35E+12	4.4839E+12	6.49E+11
σ	2.54E+10	...	9.63E+12	6.60E+11	3.3508E+12	2.74E+11
N(X)	-38.9	9.7	3.33E+11	>5.27E+13	1.51E+14	9.92E+11	—	—
σ	2.31E+10	...	7.13E+12	6.09E+11	—	—
N(X)	-17.9	9.3	3.66E+11	>4.59E+13	9.12E+13	1.41E+12	—	4.77E+11
σ	2.43E+10	...	4.30E+12	6.37E+11	—	2.53E+11
N(X)	6.4	11.7	1.66E+12	>4.84E+13	1.02E+15	2.18E+12	1.4433E+13	5.61E+12
σ	5.18E+10	...	4.82E+13	7.44E+11	4.3565E+12	4.57E+11
N(X)	25.3	9.0	8.11E+11	>3.97E+13	1.00E+14	—	8.4768E+12	1.05E+12
σ	4.13E+10	...	9.65E+12	—	3.8171E+12	3.06E+11
N(X)	45.0	10.3	2.26E+12	>5.34E+13	7.94E+14	2.35E+12	1.4673E+13	5.03E+12
σ	7.72E+10	...	3.74E+13	7.37E+11	4.2857E+12	4.29E+11
N(X)	66.2	9.9	1.01E+12	>2.26E+13	1.86E+14	—	7.1532E+12	4.73E+11
σ	4.49E+10	...	1.33E+13	—	3.7389E+12	2.97E+11
N(X)	82.6	12.4	7.07E+11	>7.75E+13	1.86E+14	—	—	2.07E+12
σ	3.46E+10	...	8.77E+12	—	—	3.46E+11
N(X)	110.3	7.7	5.63E+10	3.08E+13	6.16E+13	—	—	—
σ	1.73E+10	2.39E+12	2.91E+12	—	—	—
N(X)	129.6	8.3	—	2.05E+12	—	7.32E+11	3.1583E+12	—
σ	—	1.75E+11	—	5.52E+11	2.3436E+12	—

and Figure 5 present the resulting fits and the parameters deduced from these fits are listed in Table 4. A strong C IV doublet is also detected at $z_{\text{abs}}=1.369$ as well as a strong Mg II doublet at $z_{\text{abs}}=1.070$ in the same UVES spectrum.

Based on the profile fitting results for Mg I $\lambda 2852$, the EW is estimated to be $\text{EW}(\text{Mg I } \lambda 2852)=0.83 \pm 0.02 \text{ \AA}$, while $\text{EW}(\text{Mg II } \lambda 2796)=2.74 \pm 0.01 \text{ \AA}$, $\text{EW}(\text{Mg II } \lambda 2803)=2.62 \pm 0.01 \text{ \AA}$, $\text{EW}(\text{Zn II } \lambda 2026)=0.19 \pm 0.03 \text{ \AA}$, $\text{EW}(\text{Cr II } \lambda 2056)=0.13 \pm 0.05 \text{ \AA}$ and $\text{EW}(\text{Cr II+Zn II } \lambda 2062)=0.13 \pm 0.05 \text{ \AA}$. The broad $\lambda 2852$ absorption from 0–100 km s^{-1} in the top panel of Figure 5 would appear in the $\lambda 2026$ line of Mg I between 50 and 150 km s^{-1} of the Mg I $\lambda 2026$ panel (4th from top) as indicated by the solid vertical lines. However, the profile is remarkably free of attenuation in that velocity range. The feature at 114 km s^{-1} in Zn II $\lambda 2026$ may contain a shadow of the deepest part of the $\lambda 2852$ profile. Nevertheless, we can conclude that the contribution of Mg I to the Zn II $\lambda 2026$ line is negligible.

Mg I $\lambda 2852$ is clearly detected in this system and provides a good guidance to the velocity profile of the system. The 5 detected Fe II lines vary considerably in terms of oscillator strengths and therefore provide a fairly good determination of the total column density albeit with large error bars. In particular, the components at -17.9 and +6.4 km s^{-1} in Fe II $\lambda 2260$ are clearly blended with interlopers. Zn II and Cr II are both detected providing clear col-

umn density measurements. The determination of the column density of Zn II is based on Zn II $\lambda 2026$ while Cr II is based on the $\lambda 2056$ transition.

Finally, lines of Mn II are also present and give an accurate determination of the oscillator strength, f , and Mn column density. The resulting column densities are in excellent agreement with values derived by Khare et al. (2004) from MMT data (see Table 7 and discussion in Section 4.1). While the MMT data have higher signal-to-noise ratio, only the high resolution of the UVES observations allows one to disentangle the possible blending of lines as for example for Zn II $\lambda 2026.1$ and Mg I $\lambda 2026.5$ as in this system.

3.4 SDSS J2328+0022, $z_{\text{em}}=1.309$, $z_{\text{abs}}=0.652$

Voigt profile fitting to the Ly- α absorption line in the HST STIS spectra for this object (Rao, Turnshek & Nestor, 2006) gives $\log N_{\text{HI}}=20.32_{-0.07}^{+0.06}$. Several lines are detected in this system in the UVES spectrum, including Mg I $\lambda 2852$, Mg II $\lambda 2803$ (Mg II $\lambda 2796$ falls in a spectral gap), Fe II $\lambda\lambda 2249, 2260, 2344, 2374, 2382, 2586$ and 2600, Zn II $\lambda 2062$, Cr II $\lambda\lambda 2056$ and 2062, Mn II $\lambda\lambda 2576, 2594$ and 2606 and even Ca II K and H $\lambda\lambda 3933, 3969$. The absorption profiles show a complex velocity structure well fitted with a total of 14 components. Figure 6 and Figure 7 present the resulting fits and Table 5 the associated parameters. No lines at other

Table 5. Parameter fit to the $z_{\text{abs}} = 0.652$ SDSS J2328+0022 DLA line. Velocities and b values are in km s^{-1} and column densities are in cm^{-2} . The σ values below the column densities are the error estimates on the column densities.

	Vel	b	Mg I	Mg II	Fe II	Zn II	Cr II	Mn II	Ca II
N(X)	-82.3	3.1	4.54E+10	>1.09E+12	4.57E+11	—	1.8532E+12	—	—
σ	1.06E+10	...	3.75E+11	—	1.1182E+12	—	—
N(X)	-59.8	3.7	—	4.01E+11	—	—	1.8929E+12	1.43E+11	3.45E+10
σ	—	1.02E+11	—	—	9.2035E+11	6.49E+10	1.76E+10
N(X)	-40.7	12.3	—	1.16E+13	5.75E+12	—	3.3529E+12	7.78E+11	—
σ	—	4.90E+11	1.34E+11	—	1.8466E+12	1.00E+11	—
N(X)	-20.6	8.8	1.27E+12	>2.97E+14	5.37E+13	—	1.5493E+12	—	2.98E+11
σ	3.68E+10	...	1.25E+12	—	1.5481E+12	—	2.89E+10
N(X)	-1.6	6.0	1.08E+12	>1.72E+13	1.44E+14	1.52E+12	—	1.81E+12	6.02E+11
σ	4.28E+10	...	3.38E+12	9.86E+11	—	1.04E+11	2.94E+10
N(X)	15.3	8.7	2.44E+12	>1.23E+14	2.51E+14	—	4.0513E+12	1.90E+12	1.17E+12
σ	8.14E+10	...	5.85E+12	—	1.6278E+12	1.13E+11	3.84E+10
N(X)	35.3	9.0	1.06E+12	>2.05E+13	1.20E+14	—	1.5626E+12	9.27E+11	1.62E+11
σ	3.58E+10	...	2.80E+12	—	1.5491E+12	1.04E+11	2.84E+10
N(X)	57.6	13.1	7.99E+11	>3.15E+14	1.05E+14	—	—	1.29E+12	4.28E+11
σ	2.80E+10	...	2.44E+12	—	—	1.22E+11	3.48E+10
N(X)	85.5	10.6	4.28E+10	>4.56E+12	3.39E+12	—	—	—	—
σ	1.72E+10	...	1.59E+11	—	—	—	—
N(X)	123.2	6.1	—	5.67E+12	3.16E+12	—	1.6275E+12	9.39E+10	—
σ	—	2.36E+11	1.49E+11	—	1.3047E+12	7.66E+10	—
N(X)	140.6	4.3	—	3.23E+12	1.74E+12	—	2.3261E+12	—	—
σ	—	1.77E+11	1.24E+11	—	9.3863E+11	—	—
N(X)	154.2	6.2	—	5.00E+12	4.07E+12	1.19E+12	—	—	—
σ	—	2.16E+11	4.95E+10	9.21E+11	—	—	—
N(X)	198.1	3.9	—	7.01E+11	3.39E+11	—	4.1262E+12	—	—
σ	—	9.56E+10	9.77E+10	—	1.3373E+12	—	—
N(X)	224.1	8.1	—	1.03E+12	5.37E+11	—	—	—	—
σ	—	1.25E+11	1.24E+11	—	—	—	—

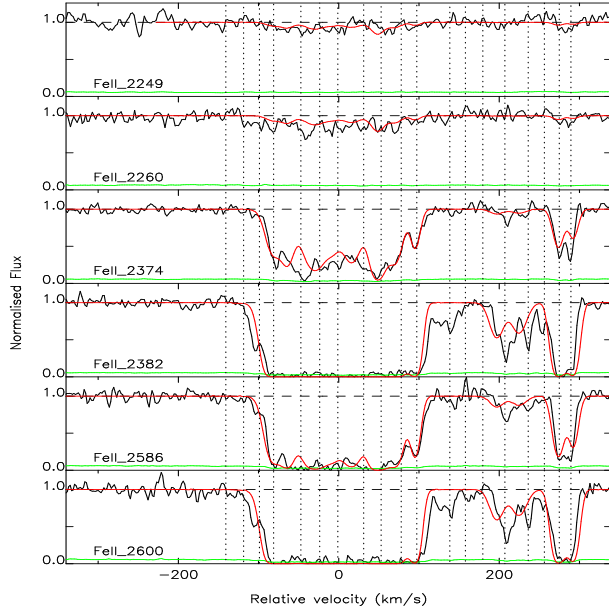


Figure 2. Velocity plots of the Fe II lines detected at $z_{\text{abs}} = 0.725$ toward SDSS J0256+0110. The dotted lines indicate positions of the components. The solid grey line near the zero flux level is the error array.

absorption redshifts are seen in either the Sloan or the UVES spectrum of that quasar.

The EW of Zn II and Cr II is bracketed assuming the whole range of velocity components seen in Mg II (this provides a $<3\sigma$ limit) on one hand and taking just the "innermost region" (which gives a $>3\sigma$ limit) on the other hand. We derive: $0.11 < \text{EW}(\text{Zn II } \lambda 2026) < 0.12 \text{ \AA}$, $0.018 < \text{EW}(\text{Cr II } \lambda 2056) < 0.022 \text{ \AA}$ and $0.05 < \text{EW}(\text{Cr II} + \text{Zn II } \lambda 2062) < 0.07 \text{ \AA}$. No shadow of Mg I $\lambda 2852$ is seen in the Zn II $\lambda 2026$ frame of Figure 7 at the expected offset position of 50 km s^{-1} for Mg I $\lambda 2026$ (solid vertical lines), once again showing that the components of $\lambda 2852$ are not saturated enough to affect our results for Zn II. Indeed, the Mg I line is clearly detected in this system and leads to a robust determination of its total column density. The weaker Fe II components at high positive and negative velocities were constrained using the $\lambda\lambda 2382, 2586$ and 2600 lines, since these components are poorly constrained by the weaker $\lambda\lambda 2249$ and 2260 lines. Zn II and Cr II are detected at $\lambda\lambda\lambda 2026, 2056$ and 2062 , respectively. Mn II is clearly detected in three different lines and leads to a robust column density determination. The Ca II $\lambda\lambda 3933$ and 3969 lines are also detected and provide a robust determination of the column densities. The rest-frame EW of these lines are measured to be: $\text{EW}(\text{Mg I } \lambda 2852) = 0.57 \pm 0.01 \text{ \AA}$, $\text{EW}(\text{Mg II } \lambda 2803) = 1.60 \pm 0.01 \text{ \AA}$, $\text{EW}(\text{Ca II } \lambda 3933) = 0.20 \pm 0.02 \text{ \AA}$ and $\text{EW}(\text{Ca II } \lambda 3968) = 0.13 \pm 0.01 \text{ \AA}$. This a case where the con-

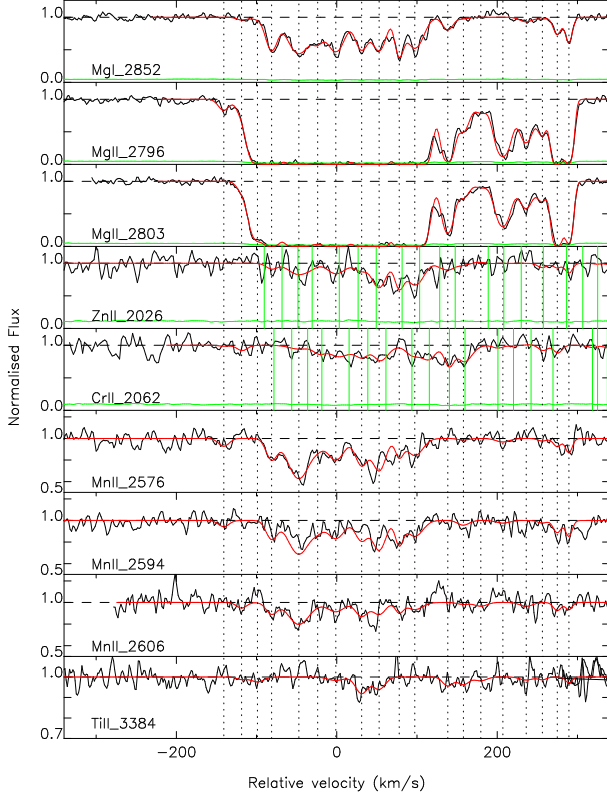


Figure 3. Velocity plots of the lines other than those of Fe II detected at $z_{\text{abs}} = 0.725$ toward SDSS J0256+0110. The dotted vertical lines indicate positions of the components while the solid vertical lines in the Zn II $\lambda 2026$ and Cr II $\lambda 2062$ panels indicate the position of the Mg I $\lambda 2026$ and Zn II $\lambda 2062$ components respectively. The solid grey line near the zero flux level is the error array.

tribution of Mg I to the Zn II $\lambda 2026$ line is probably unimportant.

4 RESULTS

4.1 Total Column Densities

The resulting total column densities for each element detected in the four quasar absorbers studied here are summarised in Table 6 together with the associated error bars. In calculating these total column densities, we used the component structure from the Fe II and Mg II lines (where all components are definitely real), but did not include the weak components listed as ‘-’ in Tables 2 to 5. Mg I, Mg II and Fe II are clearly detected in all systems, while Zn II and Cr II are only detected in three of the four systems. For comparison, we also provide $N(\text{Zn II})$ derived from a Apparent Optical Depth (AOD) method. While this provides a good consistency check that the contribution of weak components is really small compared to the contribution from the ‘core’ components, the AOD leads to an overestimate of the column densities in the presence of blends (i.e. SDSS J2328+0022). Ti II and Ca II are each detected in one quasar absorber in our sample.

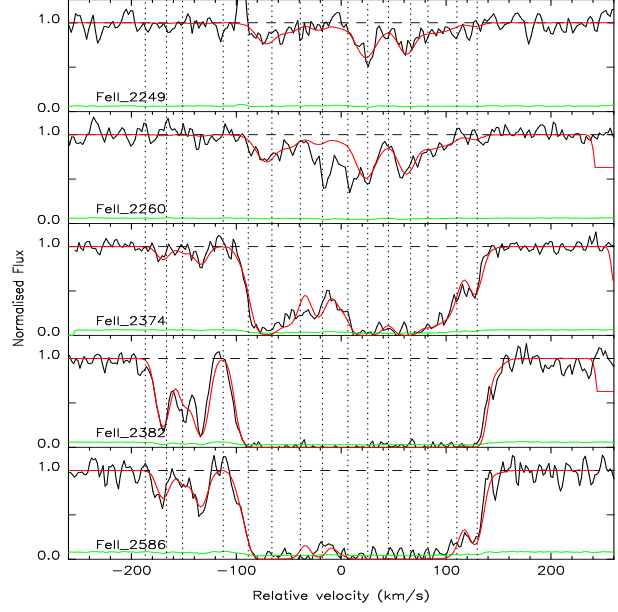


Figure 4. Velocity plots of the Fe II lines detected at $z_{\text{abs}} = 0.740$ toward SDSS J1107+0048. The dotted lines indicate positions of the components. The components at -17.9 and $+6.4$ km/s in Fe II $\lambda 2260$ are clearly blended with interlopers. The solid grey line near the zero flux level is the error array.

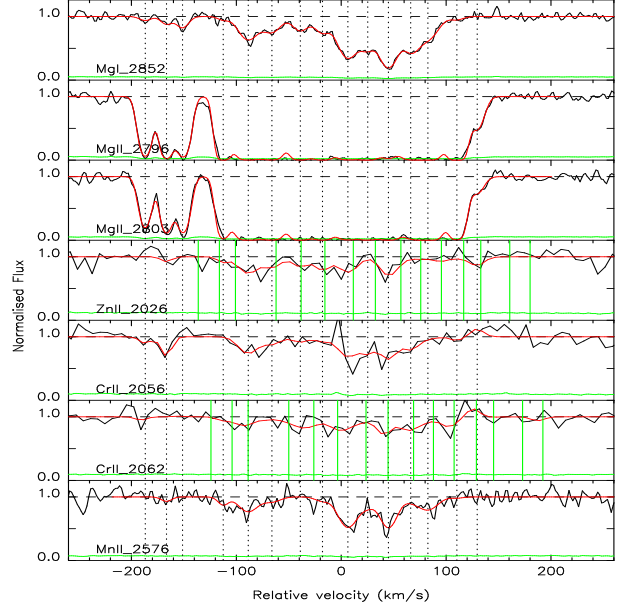


Figure 5. Velocity plots of the lines other than those of Fe II detected at $z_{\text{abs}} = 0.740$ toward SDSS J1107+0048. The dotted vertical lines indicate positions of the components while the solid vertical lines in the Zn II $\lambda 2026$ and Cr II $\lambda 2062$ panels indicate the position of the Mg I $\lambda 2026$ and Zn II $\lambda 2062$ components respectively. The solid grey line near the zero flux level is the error array.

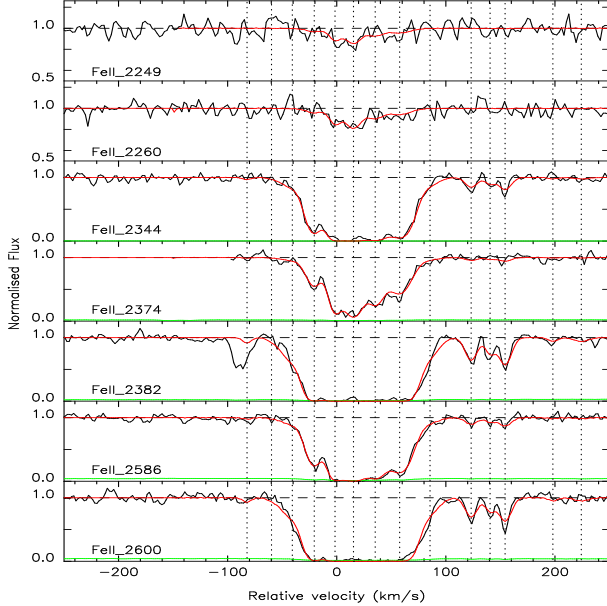


Figure 6. Velocity plots of the Fe II lines detected at $z_{\text{abs}} = 0.652$ toward SDSS J2328+0022. The dotted lines indicate positions of the components. The solid grey line near the zero flux level is the error array.

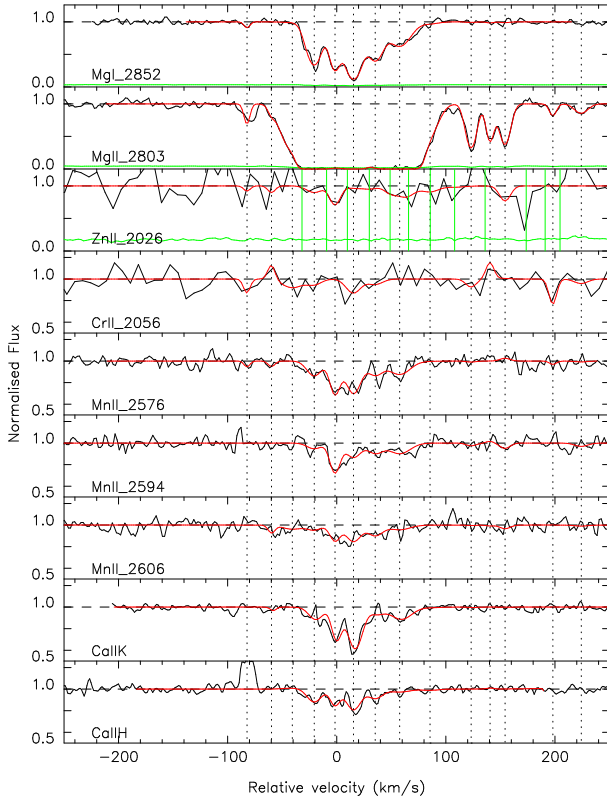


Figure 7. Velocity plots of the lines other than those of Fe II detected at $z_{\text{abs}} = 0.652$ toward SDSS J2328+0022. The dotted vertical lines indicate positions of the components while the solid vertical lines in the Zn II $\lambda 2026$ panel indicate the position of the Mg I $\lambda 2852$ components. The solid grey line near the zero flux level is the error array.

Table 7. Medium/high-resolution column densities comparison.

	SDSS J1107+0048	SDSS J0933+733	med res	high res	med res	high res
log Mg I	$12.73_{-0.82}^{+0.27}$	12.94 ± 0.01	< 12.75
log Mg II	...	> 14.73
log Fe II	$15.52_{-0.06}^{+0.06}$	15.53 ± 0.02	15.19 ± 0.01	...
log Zn II	$13.03_{-0.05}^{+0.05}$	13.06 ± 0.15	$12.67_{-0.16}^{+0.12}$	12.71 ± 0.02
log Cr II	$13.75_{-0.03}^{+0.03}$	13.84 ± 0.06	$13.46_{-0.09}^{+0.08}$	13.56 ± 0.01
log Mn II	$13.34_{-0.07}^{+0.04}$	13.27 ± 0.03	12.96 ± 0.01	...
log Ti II	< 12.82	...	$12.85_{-0.09}^{+0.21}$	< 12.43
log Co II	< 13.18	< 13.30	< 12.97	...
log Si II	$15.52_{-0.03}^{+0.03}$	> 15.55
log Ni II	$13.91_{-0.01}^{+0.01}$	13.92 ± 0.01

As often observed in high-resolution observations of quasar absorbers, one can note that the unsaturated lines of Mg II and Fe II appear near the extremes of the profiles. While this is also the case in our own Galaxy, it is still difficult to explain if no star formation took place in these regions.

Our new high-resolution results allow us to remove any doubts about anomalous abundances caused by saturation effects. In Table 7, we compare results from medium and high-resolution in two cases: the DLA with $z_{\text{abs}}=0.740$, $\log N_{\text{HI}}=21.00$ toward SDSS J1107+0048 presented in this paper and the DLA with $z_{\text{abs}}=1.479$ $\log N_{\text{HI}}=21.62$ toward SDSS J0933+733 (Khare et al. 2004; Rao, et al. 2005). The Multiple Mirror Telescope (MMT) medium-resolution spectra do not have the high resolution that characterises the UVES (SDSS J1107+0048) and Keck data (SDSS J0933+733). Still, in both cases, we find the column densities to agree well within the errors (with the exception of Cr II in SDSS J1107+0048 and Ti II in SDSS J0933+733). Nevertheless, some Zn values in the literature may be in error because of having high Mg I and not having verification of the EW(Mg I $\lambda 2852$) as an indicator of possible contamination. For instance e.g. Pettini et al. (1994), Prochaska & Wolfe (2002), Nestor et al. (2003), Khare et al. (2004) and Meiring et al. (2006) have considered Mg I contamination, whereas e.g. Prochaska & Wolfe (1999) and Prochaska et al. (2003) have not.

4.2 Abundances

The total relative abundances were calculated with respect to solar using the following formula:

$$[X/H] = \log[N(X)/N(H)]_{\text{DLA}} - \log[N(X)/N(H)]_{\odot} \quad (1)$$

where $\log[N(X)/N(H)]_{\odot}$ is the solar abundance and is taken from Asplund et al. (2005) adopting the mean of photospheric and meteoritic values for Mg, Fe, Zn, Cr, Ti, Ca and the meteoritic value for Mn. These values are recalled on the top line of Table 8. The abundance in Ca is a lower limit since the ionization potential of Ca II (11.868 eV) is lower than the one of HI and therefore Ca II represents only a portion of the total calcium contained in a neutral gas cloud.

Table 6. Total column densities for each absorber. The numbers in brackets correspond to N(Zn II) determination with Apparent Optical Depth (AOD) method. While this provides a good consistency check that the contribution of weak components is really small compared to the contribution from the 'core' components, such method leads to another estimate of the column densities in the presence of blends (i.e. SDSS J2328+0022). Ti II is detected toward SDSS J0256+0110 and Ca II toward SDSS J2328+0022.

	z_{abs}	$\log N_{\text{HI}}$	$\log N_{\text{MgI}}$	$\log N_{\text{MgII}}$	$\log N_{\text{FeII}}$	$\log N_{\text{ZnII}}$	$\log N_{\text{CrII}}$	$\log N_{\text{MnII}}$	$\log N_{\text{TiII or CaII}}$
J0134+0051	0.842	$19.93^{+0.10}_{-0.15}$	12.23 ± 0.04	>14.02	14.47 ± 0.01	$<12.17^{(11.09)}$	<12.81	<12.44	...
J0256+0110	0.725	$20.70^{+0.11}_{-0.22}$	12.97 ± 0.01	>14.83	15.13 ± 0.30	$13.19 \pm 0.04^{(13.19)}$	13.81 ± 0.05	13.24 ± 0.02	12.27 ± 0.05
J1107+0048	0.740	$21.00^{+0.02}_{-0.05}$	12.94 ± 0.01	>14.73	15.53 ± 0.02	$13.06 \pm 0.15^{(13.01)}$	13.84 ± 0.06	13.27 ± 0.03	...
J2328+0022	0.652	$20.32^{+0.06}_{-0.07}$	12.83 ± 0.01	>14.91	14.84 ± 0.01	$12.43 \pm 0.15^{(13.00)}$	13.35 ± 0.19	12.84 ± 0.02	12.43 ± 0.03

Prochaska (2003) and more recently Rodriguez et al. (2006) studied the homogeneity across the profile of the quasar absorbers using pixel analysis for high-redshift absorbers. Both these studies find the chemical abundances to be rather uniform. Here, we just compare elemental ratios in components determined by the Voigt profile fitting. Using the better-determined components in SDSS J0256+0110 and SDSS J1107+0048, we find that [Fe/Zn] varies by a factor of 5 and 6 respectively. [Fe/Mg] in the weak Mg II components and [Mn/Fe] in the strong components are found to vary by no more than a factor of 2 or 3 in all systems under study. Our findings are different from what higher redshifts have shown and might be the signature of multiple episodes of star formation.

4.3 Metal-Rich Systems

The resulting abundances for each of the systems under study are summarised in Table 8. All the absorbers are found to have metallicities larger than the N_{HI} -weighted mean metallicity for low-redshift DLAs. Overall the four quasar absorbers analysed here are amongst the most metal-rich systems known to date (see also Prochaska et al. 2006). The DLA with $\log N_{\text{HI}}=20.70$ towards SDSS J0256+0110, in particular, has an almost solar metallicity: $[\text{Zn}/\text{H}]=-0.11 \pm 0.04$. Furthermore, the sub-DLA with $\log N_{\text{HI}}=19.93$ towards SDSS J0134+0051 studied here also yields an upper limit $[\text{Zn}/\text{H}] < -0.36$ which is consistent with this absorber being a metal-rich system. These results go in line with our recent findings based on all sub-DLAs studied so far being better tracers of the metallicity of the Universe because for a given dust-to-gas ratio, there is less H I gas and therefore dust in a sub-DLA than in a DLA. Thus, the obscuration bias will affect the DLAs at a lower dust-to-gas ratio as compared to the sub-DLAs (Péroux et al., 2006). The net result is that the observed metallicity of sub-DLAs will appear higher than those of classical DLAs in a given observed limited magnitude quasar survey.

4.4 Dust Content

All the $[\text{Fe}/\text{H}]$ measurements presented here are sub-solar ($[\text{Fe}/\text{H}] \sim -1$) whilst the $[\text{Zn}/\text{H}]$ abundances determined are: $[\text{Zn}/\text{H}]=-0.11 \pm 0.04$ in SDSS J0256+0110 at $z_{\text{abs}}=0.725$, $[\text{Zn}/\text{H}]=-0.54 \pm 0.20$ in SDSS J1107+0048 at $z_{\text{abs}}=0.740$ and $[\text{Zn}/\text{H}]=-0.49 \pm 0.22$ in SDSS J2328+0022 at $z_{\text{abs}}=0.652$, plus one upper limit ($[\text{Zn}/\text{H}] < -0.36$ in

SDSS J0134+0051 at $z_{\text{abs}}=0.842$). The ratio of refractory to volatile elements, such as chromium and zinc respectively, provides an indication of the dust content of quasar absorbers (e.g. Pettini et al. 1997). An increase in the deficiency relative to the solar ratio $[\text{Cr}/\text{Zn}]=0$ corresponds to an increase in the fraction of chromium depleted from the gas to the dust phase. Here we derive $[\text{Cr}/\text{Zn}]=-0.41$ in SDSS J0256+0110, $[\text{Cr}/\text{Zn}]=-0.25$ in SDSS J1107+0048 and $[\text{Cr}/\text{Zn}]=-0.11$ in SDSS J2328+0022. So most of these systems are above the average estimate of the dust in most quasar absorbers (see Meiring et al. 2006 for a recent compilation), which is consistent with their being metal rich. These results hint once more towards the existence of a population of quasar absorbers having large amounts of dust and high Zn abundance (Vladilo & Péroux, 2005).

There have been suggestions of an obscured fraction of quasar absorbers where the dustier systems would have dimmed their background quasars to the extent that these would not be selected in abundance studies in magnitude-limited samples. Boissé et al. (1998) empirically determined a so-called "obscuration threshold" of $[\text{Zn}/\text{H}] + \log N_{\text{HI}} = \log N(\text{Zn II}) > 13.15$ in the $[\text{Zn}/\text{H}]$ versus $\log N_{\text{HI}}$ parameter space above which no quasar absorbers were observed at the time. But, there are now three DLA systems out of 65 known to lie at $\log N(\text{Zn II}) > 13.15$, and of these three DLA/sub-DLA systems only one deviates by more than 0.15 dex (SDSS J1323-0021; Péroux et al. 2006). In the sample presented here, one additional system (towards SDSS J0256+0110) is found to lie slightly above the Boissé dust cut-off. Therefore, the "obscuration threshold" reported by Boissé et al. (1998) still appears to hold empirically. It is interesting that the new points do not break the envelope by much, given that other media are known to lie in this region of the $[\text{Zn}/\text{H}]$ versus $\log N_{\text{HI}}$ plot, such as Gamma Ray Burst (GRB) hosts (see Savaglio et al. 2003, Watson et al. 2006). But it might also be that GRB hosts, which are evidently warm, high density regions, have strong Mg I and therefore overestimates of Zn II, although a curve-of-growth analysis might on the contrary underestimate Zn II.

Another mean of assessing the dust content of quasar absorbers is to look at the possible reddening of the background quasar continua. Here, we calculate the observed $g-i$ colours of the quasars and derive the excess $\Delta(g-i) = (g-i) - (g-i)_{\text{med}}$, where $(g-i)_{\text{med}}$ is the colour excess based on Sloan redshift dependent quasar composite templates (which removes the effects of redshift in the continuum and lines which affect the colors in a given band).

Table 8. Abundances with respect to solar, $[X/H]$, using the standard definition: $[X/H] = \log[N(X)/N(H)]_{DLA} - \log[N(X)/N(H)]_{\odot}$. The error bars on $[X/H]$ include both the errors in $\log N(X)$ and $\log N_{\text{HI}}$.

	z_{abs}	Mg	Fe	Zn	Cr	Mn	Ti	Ca
$A(X/N)_{\odot}$	—	-4.47	-4.55	-7.40	-6.37	-6.53	-7.11	-5.69
SDSS J0134+0051	0.842	> -1.44	-0.91 ± 0.16	< -0.36	< -0.75	< -0.96
SDSS J0256+0110	0.725	> -1.40	-1.02 ± 0.41	-0.11 ± 0.04	-0.52 ± 0.27	-0.93 ± 0.24	-1.32 ± 0.28	...
SDSS J1107+0048	0.740	> -1.80	-0.92 ± 0.04	-0.54 ± 0.20	-0.79 ± 0.11	-1.20 ± 0.08
SDSS J2328+0022	0.652	> -0.94	-0.93 ± 0.07	-0.49 ± 0.22	-0.60 ± 0.26	-0.95 ± 0.09	...	$> -0.78 \pm 0.10^a$

^a: The abundance in Ca is a lower limit since the ionisation potential of Ca II (11.868 eV) is lower than the one of HI and therefore Ca II represents only some of the total calcium contained in a neutral gas cloud.

This leads to: $\Delta(g - i) = -0.041, 0.081, 0.078$ and -0.137 for SDSS J0134+0051, SDSS J0256+0110, SDSS J1107+0048 and SDSS J2328+0022, respectively. Based on Figure 3 of York et al. (2006), if $\Delta(g - i) > 0.2$, there is a good chance that the object is reddened, while $\Delta(g - i) < 0.2$ is almost certainly not reddened (because a random sample shows few objects at those extremes). Therefore, there is no evidence for very strong reddening due to the absorbers under study in any the four quasars, but the $\Delta(g - i)$ values show that there is not inconsistency with taking the object as reddened.

4.5 D-index of Mg II Absorbers

Because N_{HI} column density estimates at low-redshift require space-based UV spectroscopy, there have been several attempts to find accurate indicators of N_{HI} from metal lines parameters with large rest-frame wavelengths (i.e. Rao, Turnshek & Nestor 2006). More recently, Ellison (2006) has proposed a finer indicator of the presence of DLAs via the so-called *D*-index, i.e. the ratio of the (Mg II $\lambda 2796$) line's EW to velocity spread. Her result shows that at fairly high-resolution N_{HI} and *D*-index correlate, with *D*-index > 6.3 corresponding to 'classical' DLAs. Our present sample adds new data to further constrain the reported correlation: Mg II $\lambda 2796$ is covered for three systems (it falls in a spectral gap for SDSS J2328+0022) plus an additional sub-DLA studied in Péroux et al. (2006). We have measured the following *D*-indices for SDSS J0134+0051, SDSS J0256+0110, SDSS J2328+0022 and SDSS J1323-0021 respectively: $D = 5.6, 6.9, 8.5$ and 7.8 . These values fall in the right ball-park of the *D*-index versus N_{HI} plot of Ellison (2006) for the SDSS J0134+0051 sub-DLA and for both the DLAs but is off in SDSS J1323-0021 case which admittedly is a sub-DLA with a large N_{HI} column density. Therefore our data confirm that the *D*-index is a good indicator of the presence of DLAs among Mg II absorbers.

4.6 Ca II Abundance at High-Resolution

Along the same line of reasoning, there has been recent renewed interest in the detection of Ca II H and K lines because they might constitute a secure tool with which to detect DLAs at low-redshift from medium-resolution optical spectra such as the ones from the Sloan Survey (Wild & Hewett, 2005; Wild, Hewett & Pettini, 2006). These authors

report a clear correlation between the strength of the Ca II equivalent width and the amount of reddening in the background quasar spectra. These findings are surprising given that Ca II is known to be highly depleted onto dust grains and that, therefore, one would expect dusty absorber to have small *measured* Ca II abundances. One way to better understand the relation between observed Ca II and dust would be to study higher-redshift quasar absorbers where the dust content can be estimated with other means (i.e. Cr II/Zn II). To our knowledge, there are very few measurements of Ca II in quasar absorbers with known $N(\text{HI})$ at high-redshift. In our sample of high-resolution spectra of $z_{\text{abs}} < 1$ quasar absorbers (Péroux et al., 2006 and the present paper), only SDSS J2328+0022 has the right wavelength coverage to allow Ca II H and K detections. Both $\lambda 3933$ and $\lambda 3969$ lines are nicely fitted at $z_{\text{abs}} = 0.652$ toward this quasar (see Figure 7) and we derive $\log N(\text{Ca II}) = 12.43 \pm 0.03$ ($[\text{Ca}/\text{H}] > -0.78 \pm 0.10$). Furthermore, we derive $[\text{Ca}/\text{Zn}] > -0.29$. More systems with a simultaneous measurement of Zn II, Cr II and Ca II lines would help to understand the origin of the trend between reddening and Ca II equivalent width.

4.7 Possible Implications for Metallicity Evolution

We now briefly discuss the implications of our data for the metallicity evolution of DLAs. Given that the selection of these systems is based on the presence of strong metal lines, these results represent a ceiling to the global metallicity evolution. This section is based on DLAs only and therefore does not include the sub-DLA towards SDSS J0134+0051 presented here or the one towards SDSS J1323-0021 (Péroux et al., 2006). The analysis is based on the statistical procedures outlined in Kulkarni & Fall (2002), and uses the data from this paper, the data compiled in Kulkarni et al. (2005), our recent MMT data (Meiring et al. 2006), and other recent data from the literature (Rao et al. 2005; Akerman et al. 2005). We binned the combined sample of 111 DLAs in 6 redshift bins with 18 or 19 systems each and calculated the global N_{HI} -weighted metallicity in each bin. Within each bin, we used Kaplan-Meier survival analysis to account for the presence of some upper limits on Zn II column densities. The N_{HI} -weighted mean metallicity in the lowest redshift bin $0.1 < z < 1.2$ is -0.79 ± 0.15 . The linear regression slope of the metallicity-redshift relation for the redshift range $0.1 < z < 3.9$ is -0.25 ± 0.07 . The

corresponding estimate for the intercept of the metallicity-redshift relation is -0.60 ± 0.16 .

Figure 8 shows these results and compares them with various models: Pei et al. (1999), Malaney & Chaboyer (1996), and Somerville et al. (2001) shown as solid, short-dashed and long-dashed curves respectively. Pei et al. (1999) used a set of equations that link the comoving densities of stars, interstellar gas, heavy elements, and dust, averaged over the whole population of galaxies to reproduce the properties of DLAs. Malaney & Chaboyer (1996) carried out chemical evolution calculations using the star formation history from Pei & Fall (1995) but without using the instantaneous recycling approximation. Somerville et al. (2001) used semi-analytic models of galaxy formation set within the cold dark matter merging hierarchy to predict the metal content of the Universe. Based on empirical relations, others (Chen et al. 2005; Zwaan et al. 2005) have argued that a combination of metallicity-luminosity relation and metallicity gradients in galaxy discs could produce lower mean metallicity at low redshift, but most models predict that the abundance of DLAs at $z=0$ should be close to solar.

For now, the current samples support the conclusions of Khare et al. (2004) and Kulkarni et al. (2005) that the metallicity of the Universe traced by DLAs evolves slowly at $z < 3$. This is clearly seen in Figure 8 which shows the N_{HI} -weighted mean metallicity *vs.* look-back time for each of our 6 redshift bins. The fact that our new systems may be biased (due to the selection criterion) towards high metallicity makes the above observations even stronger. We also calculated the N_{HI} -weighted mean metallicity in two halves of the lowest time bin since that bin encompasses a large time interval. The unfilled circles in Figure 8 refer to the lowest time bin split into 2 bins with 10 and 9 DLAs each. The points derived for these two half-bins agree very closely with the one for the corresponding combined bin. In all cases, there is a hint that the rate of metallicity evolution of DLAs may have slowed down at $z < 2$, which might be interpreted as an effect of dust obscuration. Figure 8 plotted versus age of the Universe emphasizes once more the paucity of measurements of abundances in quasar absorbers at the lowest redshifts, i.e. over the last 8 Gyr of the Universe.

5 CONCLUSIONS

To conclude, we have presented new high-resolution observations of Mg I, Mg II, Fe II, Zn II, Cr II, Mn II, Ti II and Ca II towards 3 DLAs and 1 sub-DLA at $0.6 < z_{\text{abs}} < 0.9$ selected from the Sloan Digital Sky Survey. While this small sample is not necessarily representative of the general population given the pre-selection of strong metal lines, it shows that there are high metallicity systems at $z < 1$. We now know of systems four times solar (Péroux et al. 2006) and between a half and a third solar (this work), i.e. higher than the current $z=0$ mean intercept of $1/6^{\text{th}}$ solar. In addition, our measurements more than double the sample of high-resolution Zn determinations at $z < 1$ thanks to the suitability of the blue-sensitive UVES spectrograph to these type of studies.

A comparison of high-resolution spectra with lower resolution data in a few cases where both data exist, has shown that problems of particular blends at $\lambda\lambda 2026, 2062$, and the possibility of saturation among so many components,

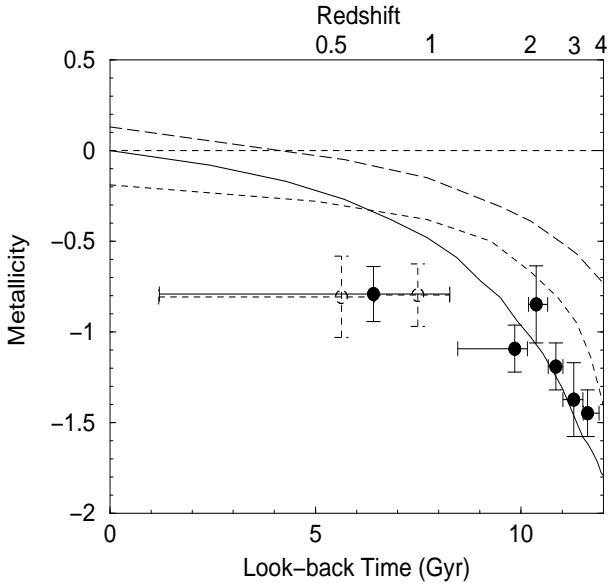


Figure 8. $N(\text{HI})$ -weighted mean Zn abundance relative to solar abundance *vs.* look-back time relation for 111 DLAs from our MMT, Magellan, VLT, and HST data and the literature. Filled circles show 6 bins with 18 or 19 DLAs each. Unfilled circles refer to the lowest time bin split into 2 bins with 9 or 10 DLAs each. Horizontal bars denote ranges in look-back times covered by each bin. Vertical error bars denote 1σ uncertainties including sampling and measurement errors. The solid, short-dashed and long-dashed curves show, respectively, the mean metallicity in the models of Pei et al. (1999), and Malaney & Chaboyer (1996), and Somerville et al. (2001). More metal-rich DLAs such as the ones reported here would be required to make the global mean metallicity of DLAs substantially deviate from sub-solar at low redshifts. For now, the time evolution of the metallicity of DLAs seem to evolve slowly at best.

do not seem to preclude getting accurate values for N_{ZnII} at lower resolution. Nevertheless, some Zn values in the literature may be in error because of not having properly addressed the potential contamination of Zn II $\lambda 2026$ with Mg I near the same wavelength. In addition, using the better-determined components in two of our systems, we find that $[\text{Fe}/\text{Zn}]$ varies by a factor of 5 and 6 respectively which is much more than what is observed in DLAs at higher redshifts.

Based on $[\text{Cr}/\text{Zn}]$ ratios and $\Delta(g-i)$ quasar continua reddening estimates, two of the four systems are found to be probably fairly dusty but interestingly only one of them marginally overcomes the Boissé et al. (1998) “obscuration threshold”. We provide further data which, for most of them, indicate that the D -index (EW of Mg II compared to velocity width) is a sharper prediction of N_{HI} than $\text{EW}(\text{Mg II})$ only. We measure the D -indices for four of our systems and find most of them to lie on the N_{HI} versus D -index correlation plot reported by Ellison (2006). In addition, we report the detection of high-resolution Ca II lines towards SDSS J2328+0022 and discuss the abundance measurement in the framework of the recent results of Wild, Hewett & Pettini (2006).

Finally, we show that relatively metal-rich systems exist

in large enough samples (see also Herbert-Fort et al. 2006), but that their impact on the overall global metallicity will only be determined with larger data samples. In particular, the possible impact of sub-DLAs on these measurements will be reviewed in a forthcoming paper (Khare et al., 2006). It is a possibility that these systems are less prone to the biasing effect of dust and thus represent the only tool currently available to detect the most metal-rich galaxies seen in absorption. More such measurements at $z < 1$ are required to be able to accurately assess the role played by these metal-rich systems in the global evolution of metals.

ACKNOWLEDGMENTS

We would like to thank the Paranal and Garching staff at ESO for performing the observations in Service Mode. JDM and VPK acknowledge partial support from the U.S. National Science Foundation grant AST-0206197 (PI: Kulkarni).

REFERENCES

Asplund, M., Grevesse, N. & Sauval, A. J., ASP Conference Series, 2005. Ed Bash & Barnes, 336, 25

Akerman, C. J., Ellison, S. L., Pettini, M. & Steidel, C. C., 2005, *A&A*, 440, 499

Boissé, P., Le Brun, V., Bergeron, J. & Deharveng, J.-M., 1998, *A&A*, 333, 841

Browne, I. W. A., Patnaik, A. R., Walsh, D. & Wilkinson, P. N., 1993, *MNRAS*, 263L, 32

Cayrel, R. et al., 2004, *A&A*, 416, 1117

Chen, H. W., Kennicutt, R. & Rauch, M., 2005, *ApJ*, 620, 703

Cohen, R., Barlow, T., Beaver, E., Junkkarinen, V., Lyons, R. & Smith, H., 1994, *ApJ*, 421, 453

de la Varga & Reimers, *A&A*, 363, 69

D'Odorico, S., Cristiani, S., Dekker, H., Hill, V., Kaufer, A., Kim, T. & Primas, F., 2000, SPIE, 4005, 121

Ellison, S., Kewley, L. & Mallén-Ornelas, G., 2005, *MNRAS*, 357, 354

Ellison, S., 2006, *MNRAS*, 368, 335

Fontana, A. & Ballester, P., 1995, *Messenger*, 80, 37.

Fukugita, M. & Peebles, P. J. E., 2004, *ApJ*, 616, 643

Hall, P. B., Richards, G. T., York, D. G., Keeton, C. R., Bowen, D. V., Schneider, D. P., Schlegel, D. J. & Brinkmann, J., 2002, *ApJ*, 575L, 51

Herbert-Fort, S., Prochaska, J., Dessauges-Zavadsky, M., Ellison, S., Howk, J. C., Wolfe, M. A. & Prochter, G. E., 2006, *PASP*, *astro-ph/0607430*

Khare, P., Kulkarni, V. P., Lauroesch, J. T., York, D. G., Crotts, A. P. S. & Nakamura, O., 2004, *ApJ*, 616, 86

Khare, P., Kulkarni, V. P., Péroux, C., York, D. G., Lauroesch, J. T. & Meiring, J. D., 2006, *MNRAS*, submitted

Kulkarni, V. P., Fall, S. M. & Truran, J. W., 1997, *ApJ*, 484, L7

Kulkarni, V. P. & Fall, S. M., 2002, *ApJ*, 580, 732

Kulkarni, V. P., Fall, S. M., Lauroesch, J. T., York, D. G., Welty, D. E., Khare, P. & Truran, J. W., 2005, *ApJ*, 618, 68

Malaney, R. A. & Chaboyer, B., 1996, *ApJ*, 462, 57

Meiring, J. D., Kulkarni, V. P., Khare, P., Bechtold, J., York, D. G., Cui, J., Lauroesch, J. T., Crotts, A. P. S. & Nakamura, O., 2006, *MNRAS*, submitted

Meyer, D. & York, D., 1992, *ApJ*, 399L, 121

Mishenina, T. V., Kovtyukh, V. V., Soubiran, C., Travaglio, C. & Busso, M., 2002, *A&A*, 396, 189

Morton, D. C., 2003, *ApJS*, 149, 205

Nestor, D., Rao, S., Turnshek, D. & Vanden Berk, D., 2003, *ApJ*, 595L, 5

Pei, Y. C., Fall, S. M. & Hauser, M. G., 1999, *ApJ*, 522, 604

Péroux, C., Petitjean, P., Aracil, B. & Srianand, A., 2002, *New A.*, 7, 577

Péroux, C., McMahon, R., Storrie-Lombardi, L., & Irwin, M., 2003, *MNRAS*, 346, 1103

Péroux, C., Kulkarni, V. P., Meiring, J., Ferlet, R., Khare, P., Lauroesch, J. T., Vladilo, G. & York, D. G., 2006, *A&A*, Petitjean, P., Aracil, B., Srianand, R. & Ibata, R., 2000, *A&A*, 359, 457

Pettini, M., King, D. L., Smith, L. J. & Hunstead, R. W., 1997, *ApJ*, 478, 536

Pettini, M., Smith, L. J., Hunstead, R. W. & King, D. L., 1994, *ApJ*, 426, 79P

Pettini, M., Ellison, S. L., Steidel, C. C., Shapley, A. E. & Bowen, D. V., 2000, *ApJ*, 532, 65.

Prochaska, J., Gawiser, E., Wolfe, A. M., Castro, S. & Djorgovski, S. G., 2003, *ApJ*, 595L, 9

Prochaska, J. X. & Wolfe, A., 2002, *ApJ*, 566, 68

Prochaska, J. X. & Wolfe, A., 1999, *ApJS*, 121, 369

Prochaska, J. X., Gawiser, E., Wolfe, A., Castro, S., Djorgovski, S.G., 2003, *ApJ*, 595, 9

Prochaska, J. X., O'Meara, J., Herbert-Fort, S., Burles, S., Prochter, G. E. & Bernstein, R. A., 2006, *ApJL*, *astro-ph/0606573*

Rao, S., Prochaska, J., Howk, C. & Wolfe, A., 2005, *AJ*, 129, 9

Rao, S. M., Turnshek, D. A., & Nestor D. B., 2006, *ApJ*, 636, 610

Richards, G., 2001, *ApJ*, 121, 2308

Rodriguez, E., Petitjean, P., Aracil, B., Ledoux, C. & Srianand, R., 2006, *A&A*, 446, 791

Routly, P. & Spitzer, L., 1952, *ApJ*, 115, 227

Savaglio, S., Fall, S. M., & Fiore, F. 2003, *ApJ*, 585, 638

Savaglio, S. et al., 2005, *ApJ*, 635, 260

Tremonti, C. et al., 2004, *ApJ*, 613, 898

Vidal-Madjar, A., Laurent, C., Bonnet, R. M., & York, D. G. 1977, *ApJ*, 211, 91

Vladilo, G. & Péroux, C., 2005, *A&A*, 444, 461

Welty, D. E., Hobbs, L. M., & York, D. G. 1991, *ApJS*, 75, 425

York, D. G. and the SDSS Collaboration, 2000, *AJ*, 120, 1579

York, D. G. and the SDSS Collaboration, 2001, *BAAS*, 198, 78.

York, D. G. et al., 2005, “Probing Galaxies through Quasar Absorption Lines”, IAU Colloquium Proceedings of the International Astronomical Union 199, Shanghai, Ed. P. R. Williams, C.-G. Shu and B. Ménard.

York, D. G. et al., 2006, *MNRAS*, 367, 945

Watson, D. et al., 2006, *ApJ*, submitted, *astro-ph/0510368*

Wang, T.G., Dong, X.B., Zhou, H. Y. & Wang, J. X., 2005, *ApJ*, 622, L101

Wild, V. & Hewett, P., 2005, *MNRAS*, 361L, 30

Wild, V., Hewett, P. & Pettini, M., 2005, *MNRAS*, 367, 211

Zwaan, M., van der Hulst, J. M., Briggs, F. H., Verheijen, M. A. & Ryan-Weber, E. V., 2005, *MNRAS*, 364, 1467